

1 **A New Stefan Equation to Characterize the Evolution of Thermokarst**
2 **Lake and Talik Geometry**

3 **Noriaki Ohara¹, Benjamin M. Jones², Andrew D. Parsekian^{3,1}, Kenneth M. Hinkel⁴, Katsu**
4 **Yamatani⁵, Mikhail Kanevskiy², Rodrigo C. Rangel³, Amy L. Breen⁶, and Helena**
5 **Bergstedt^{2,7}**

6

7 ¹Department of Civil and Architectural Engineering, University of Wyoming, Laramie, WY,
8 82071, USA

9 ²Institute of Northern Engineering, University of Alaska Fairbanks, Fairbanks, Alaska, 99775,
10 USA

11 ³Department of Geology and Geophysics, University of Wyoming, Laramie, WY 82071, USA

12 ⁴Department of Geological and Mining Engineering and Sciences, Michigan Technological
13 University, Houghton, MI 49931, USA

14 ⁵Department of Urban Science, Meijo University, 4-102-9 Yataminami, Higashi, Nagoya 461-
15 8534, Japan

16 ⁶International Arctic Research Center, University of Alaska Fairbanks, Fairbanks, Alaska

17 ⁷b.geos, Vienna, Austria

18 Corresponding author: Noriaki Ohara (nohara1@uwyo.edu)

19

20 **Abstract**

21 Thermokarst lake dynamics, which play an essential role in carbon release due to permafrost
22 thaw, are affected by various geomorphological processes. In this study, we derive a three-
23 dimensional (3D) Stefan equation to characterize talik geometry under a hypothetical
24 thermokarst lake in the continuous permafrost region. Using the Euler equation in the calculus
25 of variations, the lower bounds of the talik were determined as an extremum of the functional
26 describing the phase boundary area with a fixed total talik volume. We demonstrate that the
27 semi-ellipsoid geometry of the talik is optimal for minimizing the total permafrost thaw under
28 the lake for a given annual heat supply. The model predicting ellipsoidal talik geometry was
29 compared to talik thickness observations using transient electromagnetic (TEM) soundings in
30 Peatball Lake on the Arctic Coastal Plain (ACP) of northern Alaska. The width-depth ratio of the
31 elliptical sub-lake talik can characterize the energy flux anisotropy in the permafrost, although
32 the lake bathymetry cross section may not be elliptic due to the presence of near-surface ice-rich
33 permafrost. This theory suggests that talik development deepens lakes and results in more
34 uniform horizontal lake expansion around the perimeter of the lakes while wind-induced waves
35 and currents are likely responsible for the elongation and orientation of shallow thermokarst
36 lakes without taliks in certain regions such as the ACP of northern Alaska.

37 **1. Introduction**

38 Thermokarst lakes are abundant in regions underlain by ice-rich permafrost including the Arctic
39 Coastal Plain (ACP) of northern Alaska, northwestern Canada, and Siberia (Grosse et al., 2013;
40 Jones et al., 2022). These lakes are formed due to permafrost degradation, and their basin
41 evolution is fundamentally different from lakes formed in temperate and tropical regions.
42 Thermokarst lakes affect the thermal regime of the surrounding permafrost, which controls the
43 geomorphology and evolution of the lake basin (Brewer, 1958). If the lake bed has a mean
44 annual temperature greater than 0 °C, the sub-lake permafrost will begin to thaw (Burn, 2002; Arp
45 et al., 2016). This typically occurs in lakes that are deeper than the maximum winter ice
46 thickness, where the ice cover floats above an unfrozen water layer (Jeffries et al., 1996; Burn,
47 2002). In this case, unfrozen lake bed sediments persist, and the thaw front continues to
48 penetrate deeper into the underlying permafrost. This results in a “talik”, or a perpetually
49 unfrozen zone confined by permafrost, beneath the lake depending on local anomalies in
50 thermal, hydrological, hydrogeological, or hydrochemical conditions (van Everdingen, 1998). In
51 ice-rich permafrost, the conversion of ice to water with thaw causes a volumetric reduction in the
52 unconsolidated material, and the lake bed consequently subsides significantly increasing the
53 depth of initial basins (Czudek and Demek, 1970; Jorgenson and Shur, 2007; Shur and
54 Osterkamp, 2007; Jorgenson, 2013; French, 2018). The total depth of thaw subsidence is
55 determined by the amount and distribution of excess-ice content in the permafrost with depth. As
56 the lake expands by lateral thermo-mechanical erosion of the banks, mineral and organic
57 sediments from retreating shores are delivered to the lake basin (Farquharson et al., 2016).
58 However, thaw-induced ground subsidence effectively deepens the basin, so volumetric capacity

59 can increase over time. Over decades and centuries, the talik increases in thickness, and lake bed
60 subsidence continues as long as the thawing permafrost is ice-rich (West and Plug, 2008).

61 In certain ice-rich permafrost regions in the Arctic, there is a preferential orientation and elliptic
62 shape to the thermokarst lakes (Black and Barksdale, 1949; Hinkel et al., 2005; Grosse et al.,
63 2013). In particular, elliptical oriented lake districts are found predominantly along the central
64 north Siberian coast, northern Alaska and in northwest Canada (Grosse et al., 2013). On the
65 ACP of northern Alaska, many elliptical thermokarst lakes have a long axis oriented 10–20
66 degrees west from true north, which is nearly perpendicular to the prevailing wind direction
67 (Carson, 1968; Sellmann, 1975; Carter, 1981). Hinkel et al. (2005, 2012) also showed
68 significant correlation between lake orientation and summer wind direction by analyzing the
69 geometric shape metrics of the thermokarst lakes and drained thermokarst lake basins (DTLB)
70 on the ACP of Alaska. It has been proposed that winds at the lake surface cause currents and
71 water waves, which trigger thermomechanical bank erosion, resulting in asymmetrical elliptical
72 orientation (Livingstone, 1954; Rex, 1961; Carson and Hussey, 1962; Mackay, 1992; Arp et al.,
73 2011). The sublittoral shelves and bars typically found in the deeper thermokarst lakes may also
74 be formed by wind-driven currents and waves, and warmer water temperatures (Carson and
75 Hussey, 1962). The axis-oriented sublittoral shelves make the orientation appear more
76 pronounced in larger basins. Other processes also influence the orientation of thermokarst lakes
77 such as historical drained lake geometry, ground ice distribution, and dune ridge orientation by
78 aeolian sand transport (Carter, 1981).

79 Several numerical models have been proposed and applied that describe permafrost thaw for the
80 purpose of analyzing water and carbon cycles (e.g., Kessler et al., 2012). However, Schuur et al.
81 (2015) stress the need to better represent talik formation and geometries to parameterize

82 numerical models more effectively. Painter et al. (2016) demonstrated a coupled
83 surface/subsurface permafrost thermal hydrology model at the multiple ice-wedge polygon scale.
84 Kessler et al. (2012) simulated carbon mobilization over 10,000 years on two neighboring thaw
85 lakes located on ice- and organic-rich Yedoma permafrost terrain (Kanevskiy et al., 2011;
86 Schirrmeister et al., 2013) in the northern Seward Peninsula, Alaska using a 3D numerical
87 thermal model. They demonstrated the effectiveness of model simulations for methane emission
88 from thermokarst lakes. Ling and Zhang (2003b) provided a numerical parametrization of lake
89 talik development and showed that shallow thermokarst lakes are a significant heat source
90 affecting permafrost and talik geometries. Rowland et al. (2011) advanced the technique by
91 including advective heat transport on talik evolution. West and Plug (2008) and Plug and West
92 (2009) characterized the lake bathymetry including the effects of lake ice and littoral shelves.
93 These thermal models use long-term mean lake temperature as the Dirichlet boundary condition
94 and a uniform annual mean temperature profile as the initial condition. Analytical and numerical
95 models can provide dynamic solutions for the heat transfer equation under quasi-steady state
96 climate conditions. However, the existing models require prescribed lake shapes (circle or
97 ellipse) to obtain information on talik depths as opposed to modeling the likely influence of talik
98 evolution on lake shape – this work, in part, attempts to address this shortcoming.

99 Direct drilling measurements of taliks below thermokarst lakes are difficult to obtain and only
100 exist in a few rare case studies (Brewer, 1958; Johnston and Brown, 1966; Roy-Leveillee and
101 Burn, 2017; Heslop et al., 2015). Geophysical methods can be used (e.g., Schwamborn et al.,
102 2000; Parsekian et al., 2019; Creighton et al., 2018; Sullivan et al., 2021; O’Neill et al., 2020);
103 however, it is time consuming and laborious to produce 3D subsurface images at the large scale
104 of lakes found in permafrost lowland regions. Since field measurements (coring, geophysics,

105 etc.) are spatiotemporally limited, numerical and analytical modelling is used to gain critical
106 insights into talik evolution. Mackay (1962) obtained the analytical vertical temperature profiles
107 below the water at the center of a circular lake by analytically solving the heat transfer equation.
108 Burn (2002) subsequently extended the solution for an elongated lake. This analytical model has
109 been used for lake process characterization because the quasi-steady state model was able to
110 reasonably quantify the talik thickness. For example, Hinkel and Arp (2015) applied the
111 temperature profile to 2100 lakes and found that larger, long-lived lakes (more than 66 ha) may
112 have taliks that penetrate through the permafrost (open taliks) to the ground-water system below
113 in a region with permafrost that is up to 600 m thick.

114 These existing models require the prescribed lake shapes (circle or ellipse) to obtain the talik
115 depth; in fact, no existing studies explicitly provide an answer to the fundamental question: why
116 do thermokarst lakes tend to be elliptical and/or round? Also, in spite of several decades of
117 research focused on the orientation of thermokarst lakes in certain regions, no existing studies
118 explicitly explain why thermokarst lakes in some regions orient perpendicular to the prevailing
119 wind direction. The objective of this work is to implement a novel mathematical framework that
120 concurrently describes both the oriented nature of the thermokarst lakes and the talik depth
121 below the lakes. Previous models have calculated the talik development due to heat flow, though
122 most use some simplifying assumptions to reduce dimensionality. Separately, researchers have
123 hypothesized about elliptical lake morphology by invoking winds, currents, and erosion. Here,
124 we couple both the talik evolution and lake shape questions together in a single mathematical
125 model. Additionally, we intend to use this theory to demonstrate that the thermal gradient could
126 exert control on the depth/width ratio of the talik. In other words, the proposed theory aims to
127 isolate the most important process – sub-lake permafrost thaw and subsidence – from other

128 effects such as wind-wave erosion, thaw slumping, sediment redistribution and incoming
129 radiation imbalance, using thermally optimized lake geometry.

130 **2. Theory**

131 **2.1 Basin integrated energy equation**

132 The approach used in this study is based on Lagrangian mechanics, which generalizes the
133 classical Newtonian mechanics, using the stationary action principle (the principle of least
134 action). The action is defined as the integral of the Lagrangian, which consists of kinetic and
135 potential energy of the system. In this application, the Lagrangian simply becomes the potential
136 energy due to absence of kinetic energy. The variational principle that is the main tool in
137 Lagrangian mechanics can indeed derive the equations in Newtonian mechanics. One of the
138 related research topics using the variational principle to fluid mechanics is phase boundary
139 propagation, which can be analyzed by the phase field model or diffusion-interface model
140 (Cassel, 2013). This model explains the diffuse phase boundary without surface tension that
141 appears in Newtonian interfacial physics between a liquid and a gas. According to the second
142 law of thermodynamics, the free energy of the system must decrease monotonically to ensure a
143 non-negative entropy production (Singer-Loginova and Singer, 2008). This requires that the time
144 rate of change of the phase boundary be expressed by the functional derivative of the free energy
145 functional, which corresponds to the total energy flux into the talik in relation to permafrost
146 thaw. This study directly and analytically solves the Euler-Lagrange equation based on the
147 stationary action principle rather than the entropy functional used in the phase field method.
148 Heat energy collected by a waterbody is used for phase boundary expansion as well as heat
149 conduction into the adjacent permafrost (e.g., French, 2018). From the energy balance equation

150 around the phase boundary, the energy for permafrost thaw is expressed as the subtraction of
 151 heat conduction from the input energy at the phase boundary (Carslaw and Jaeger, 1959; Patel,
 152 1968; Lunardini, 1981). The material of permafrost and talik is assumed to be fully saturated
 153 with ice and water, respectively. Also, the thermal constants (thermal conductivity, latent heat,
 154 and thawing temperature) are constant and isotropic, and the change in volume of water on
 155 thawing and freezing is negligible. Under such assumptions, the energy conservation equation at
 156 the phase boundary can be expressed as,

$$157 \quad \phi v \rho L = q_{suf} - k_L \frac{dT}{dn} - \left(-k_p \frac{dT}{dn} \right) \quad , \quad (1)$$

158 where ϕ is volumetric water content (m^3/m^3); v is thaw rate or advancement of talik boundary
 159 (m/s); ρ is density of water (kg/m^3); L is latent heat for ice thaw (liquid-solid) (J kg^{-1}); q_{suf} is
 160 additional heat input from ground surface around the lake shore (W/m^2); k_L is thermal
 161 conductivity of unfrozen soil ($\text{W}/(\text{m}\cdot\text{C})$); and k_p is thermal conductivity of frozen soil
 162 (permafrost) ($\text{W}/(\text{m}\cdot\text{C})$); T is temperature (C); and n is outward normal from the interface into
 163 the soil (m). The energy terms can be grouped into heat for permafrost thaw, q_{th} (W/m^2);
 164 incoming heat at the phase boundary q_{in} (W/m^2); and outgoing heat by conduction to the
 165 permafrost q_{out} (W/m^2). These heat fluxes can be evaluated by the following formulas:

$$166 \quad q_{th} = \phi v \rho L \quad , \quad (2)$$

$$167 \quad q_{in} = q_{suf} - k_L \frac{dT}{dn} \quad , \text{ and} \quad (3)$$

$$168 \quad q_{out} = -k_p \frac{dT}{dn}. \quad (4)$$

169 When heat input from the surface is consumed for phase change without any loss ($q_{out} = q_{suf} =$
170 0), the well-known Stefan equation can be obtained from Equations (1) through (4) under the
171 quasi-steady state approximation (Stefan, 1891; Kurylyk & Hayashi, 2016). This study also
172 adopts the quasi-steady state approximation for the talik shape characterization.
173 As the thawing process is direction-dependent, it is convenient to use vector notation (Figure 1).
174 That is,

$$175 \quad \mathbf{q}_{th} = \mathbf{q}_{in} - \mathbf{q}_{out} \quad . \quad (5)$$

176 A vector is denoted by a bold letter. The talik expansion flux vector corresponds to thaw
177 direction, which is affected by the other two heat fluxes. Figure 1 illustrates the thermal profiles
178 around the thaw lake in warm and cold seasons. The horizontal near-surface heat conduction is
179 influenced by the seasonality of the surface heat budget while the vertical heat conduction under
180 the lake remains unidirectional throughout the years. Clearly, the presence of the thaw lake
181 considerably alters the heat environment of the permafrost while the temperature slope at the
182 bottom of the permafrost may be approximated by the geothermal gradient in regions with thick
183 continuous permafrost such as the ACP. This directionality in the heat environment around the
184 lake may cause anisotropic talik expansion. Here, the phase change heat vector is expressed as
185 proportional to the normal heat input q_{in} , as follows:

$$186 \quad \mathbf{q}_{th} = (q_{th,x}, q_{th,y}, q_{th,z}) = (\xi q_{in}, \eta q_{in}, \zeta q_{in}) = q_{in}(\xi, \eta, \zeta) \quad (6)$$

187 where q_{in} is the input heat normal to the phase boundary, $\xi, \eta,$ and ζ are the thaw energy
188 fractions of the heat input normal to the phase boundary with respect to x, y, and z directions,
189 respectively. The depth of the phase boundary (m) , $z = \varphi(x, y)$, may be expressed as an
190 arbitrary 3D surface as,

191
$$g(x, y, z) = \varphi(x, y) - z = 0. \quad (7)$$

192 Hence, the normal vector \mathbf{n} at any location on the phase boundary g can be written as follows:

193
$$\mathbf{n} = \frac{\nabla g}{|\nabla g|} = \frac{1}{|\nabla g|} (g_x, g_y, g_z) = \frac{1}{\sqrt{\varphi_x^2 + \varphi_y^2 + 1}} (\varphi_x, \varphi_y, -1) \quad (8)$$

194 where the subscript in this expression denotes partial derivative (e.g. $\varphi_x = \partial\varphi/\partial x$) and ∇ is a
 195 vector differential operator ($\partial/\partial x, \partial/\partial y, \partial/\partial z$). As such, the vector of the input heat to the
 196 phase boundary φ is

197
$$\mathbf{q}_{in} = |\mathbf{q}_{in}| \mathbf{n} = q_{in} \mathbf{n} = \frac{q_{in}}{\sqrt{\varphi_x^2 + \varphi_y^2 + 1}} (\varphi_x, \varphi_y, -1), \quad (9)$$

198 and the corresponding thaw heat vector is,

199
$$\mathbf{q}_{th} = \frac{q_{in}}{\sqrt{\varphi_x^2 + \varphi_y^2 + 1}} (\xi\varphi_x, \eta\varphi_y, -\zeta). \quad (10)$$

200 Next, the thaw heat magnitude can be evaluated using a Euclidian norm as,

201
$$|\mathbf{q}_{th}| = \frac{q_{in}}{\sqrt{\varphi_x^2 + \varphi_y^2 + 1}} \sqrt{\xi^2\varphi_x^2 + \eta^2\varphi_y^2 + \zeta^2} = \frac{\zeta q_{in}}{\sqrt{\varphi_x^2 + \varphi_y^2 + 1}} \sqrt{\alpha_x^2\varphi_x^2 + \alpha_y^2\varphi_y^2 + 1} \quad (11)$$

202 where

203
$$\alpha_x = \frac{\xi}{\zeta}, \quad \alpha_y = \frac{\eta}{\zeta}. \quad (12)$$

204 The parameters α_x and α_y (unitless ratio) describe the anisotropic thermal condition between
 205 horizontal and vertical directions. The parameters α_x and α_y are greater than one when the
 206 vertical temperature gradient is steeper than in horizontal gradient. The total thaw energy over
 207 the lake can be computed by the area integral on the phase boundary Γ . That is,

$$\begin{aligned}
208 \quad \int_{\Gamma} |\mathbf{q}_{th}| d\Gamma &= \iint_B |\mathbf{q}_{th}| \sqrt{\varphi_x^2 + \varphi_y^2 + 1} dx dy \\
209 \quad &= \zeta q_{in} \iint_B \sqrt{\alpha_x^2 \varphi_x^2 + \alpha_y^2 \varphi_y^2 + 1} dx dy. \quad (13)
\end{aligned}$$

210 This expression indicates that the heat required for lake expansion is proportional to the weighted
211 phase boundary area with the weights α_x and α_y .

212 **2.2 Optimum phase boundary shape**

213 The calculus of variation, often referred to as a functional analysis, is the mathematical technique
214 to find an extremum (minimum or maximum) of the system in terms of a function type instead of
215 a variable (e.g., Courant and Hilbert, 1954; Gelfand and Fomin, 1963). Thermally optimum
216 function types $\varphi(x, y)$ of the phase boundary can be derived using this method. As presented in
217 the previous section, the heat consumption rate for talik expansion is represented by the weighted
218 phase boundary area while the time-integrated heat supply is equivalent to the thawed permafrost
219 volume. Assuming heat thaws the most susceptible region of the permafrost near the heat source
220 first, the shape of a talik may minimize the total permafrost thaw with a given amount of
221 incoming energy. In other words, as the free energy of the system must decrease monotonically
222 to ensure a non-negative entropy production (the second law of thermodynamics), the optimum
223 talik shape should minimize the phase boundary area for a specified talik volume. The weighted
224 phase boundary area A and its volume V can be expressed as follows:

$$225 \quad \begin{cases} V[\varphi] = \iint_B \varphi dx dy \\ A[\varphi] = \iint_B \sqrt{\alpha_x^2 \varphi_x^2 + \alpha_y^2 \varphi_y^2 + 1} dx dy \end{cases} \quad (14)$$

226 To obtain the optimum talik shape, the functional F is formulated using the method of Lagrange
227 multipliers as,

228
$$F[\varphi] = \lambda V[\varphi] + A[\varphi] = \iint_B (\lambda \varphi + \sqrt{\alpha_x^2 \varphi_x^2 + \alpha_y^2 \varphi_y^2 + 1}) dx dy \quad (15)$$

229 where λ is the Lagrange multiplier. The minimum of the functional F can be determined for $\lambda <$
 230 0 because both V and A are monotonic functions. Let

231
$$f(\varphi, \varphi_x, \varphi_y) = \lambda \varphi + \sqrt{\alpha_x^2 \varphi_x^2 + \alpha_y^2 \varphi_y^2 + 1}. \quad (16)$$

232 Equation (15) becomes,

233
$$F[\varphi] = \lambda V[\varphi] + A[\varphi] = \iint_B f(\varphi, \varphi_x, \varphi_y) dx dy. \quad (17)$$

234 Note that this functional can be interpreted as the Lagrangian of the system. Therefore, to find
 235 the extremal phase-boundary shape φ that minimizes the functional $F[\varphi]$, the Euler-Lagrange
 236 equation can be formulated as,

237
$$\frac{\partial f(\varphi, \varphi_x, \varphi_y)}{\partial \varphi} - \frac{\partial}{\partial x} \left(\frac{\partial f(\varphi, \varphi_x, \varphi_y)}{\partial \varphi_x} \right) - \frac{\partial}{\partial y} \left(\frac{\partial f(\varphi, \varphi_x, \varphi_y)}{\partial \varphi_y} \right) = 0. \quad (18)$$

238 Substituting Equation (16) to (18) yields,

239
$$\lambda - \frac{\partial}{\partial x} \left(\frac{\alpha_x^2 \varphi_x}{\sqrt{1 + \alpha_x^2 \varphi_x^2 + \alpha_y^2 \varphi_y^2}} \right) - \frac{\partial}{\partial y} \left(\frac{\alpha_y^2 \varphi_y}{\sqrt{1 + \alpha_x^2 \varphi_x^2 + \alpha_y^2 \varphi_y^2}} \right) = 0. \quad (19)$$

240 By analogy to two-dimensional application in Ohara and Yamatani (2019), an ellipsoid is one of
 241 the solutions of Equation (19), as follows:

242
$$z = -\varphi = -\sqrt{\frac{4}{\lambda^2} - \frac{x^2}{\alpha_x^2} - \frac{y^2}{\alpha_y^2}} + d, \text{ or} \quad (20)$$

243
$$\left(\frac{x}{\frac{2\alpha_x}{|\lambda|}} \right)^2 + \left(\frac{y}{\frac{2\alpha_y}{|\lambda|}} \right)^2 + \left(\frac{z-d}{\frac{2}{|\lambda|}} \right)^2 = 1. \quad (21)$$

244 Detailed alternative derivation using isoperimetric inequality is available in the Appendix A. The
 245 coefficients d and λ can be determined by further variational analysis explained in Appendix B.
 246 As such, Equations (20) and (21) become

$$247 \quad \varphi = \sqrt{D^2 - \frac{x^2}{\alpha_x^2} - \frac{y^2}{\alpha_y^2}}, \text{ and} \quad (22)$$

$$248 \quad \left(\frac{x}{\alpha_x D}\right)^2 + \left(\frac{y}{\alpha_y D}\right)^2 + \left(\frac{z}{D}\right)^2 = 1, \text{ respectively.} \quad (23)$$

249 D is the talik center depth, α_x & α_y are the cross-sectional aspect ratios. Hence, the semi-
 250 ellipsoidal geometry of the phase boundary (i.e., the boundary between the permafrost and talik)
 251 was explicitly derived as a thermally optimum shape based on the variational principle using the
 252 thermal quasi-steady state approximation. This result is consistent with the existing numerical
 253 thermal models (Schwamborn et al., 2000; Plug and West, 2009; Ling and Zhang, 2003b;
 254 Kessler et al., 2012) which predicted nearly elliptic talik cross sections under thaw lakes in a
 255 continuous permafrost. As the Stefan equation describes the phase boundary depth (active layer
 256 depth or frost depth) under a uniform and flat landscape, the solution of the Euler-Lagrange
 257 equation (Equation 22) is the 3D Stefan Equation for the talik beneath a thermokarst lake.

258 **2.3 Thermokarst lake bathymetry and phase boundary geometry**

259 When top-down permafrost thaw dominates the process, the thermokarst lake bottom shape
 260 $\psi(x, y)$ may be similar to the phase boundary shape, as illustrated in Figure 2. However, the
 261 lake bathymetry can be related to the permafrost degradation rate r_{deg} (ratio; m/m) defined as,

$$262 \quad r_{deg} = \frac{D_{thaw}}{D_{frzn}} \sim 1 - \frac{\psi(x,y)}{\varphi(x,y)} \sim 1 - \frac{H}{D} \quad , \quad (24)$$

263 where H and D denote the water depth and the talik thickness at the lake center, respectively.
264 D_{frzn} is the frozen soil thickness (m) and D_{thaw} is the corresponding thawed soil thickness depth
265 (m), which is strongly dependent on the excess ground ice content; excess ice is defined as the
266 volume of ice in the ground, which exceeds the total pore volume that the ground would have
267 under natural unfrozen conditions (van Everdingen, 1998). Therefore, thaw settlement is
268 typically computed from excess-ice content and the thickness of the layer with excess ground
269 ice. However, as the consolidation settlement effect, which is a function of void ratio and
270 effective stress, may not be separated, we use the simple permafrost degradation rate (Equation
271 24) in this study.

272 If the permafrost degradation rate is uniform and constant throughout the basin (Panel A:
273 uniform permafrost in Figure 2), the lake bathymetry tends to be an ellipsoid shape. However, as
274 the ice-rich layer is typically developed near the surface on the ACP (e.g., Kanevskiy et al.,
275 2011, 2013), the bathymetry may have a flatter bottom like a rectangular cross section (Panel B:
276 layered permafrost in Figure 2) because the ice-rich layer is characterized by much higher thaw
277 settlement than the ice-poor permafrost at depth. Therefore, proportionality between talik
278 thickness and lake water depth is unlikely reasonable assumption due to the ice-rich layer
279 presence. Indeed, Hinkel et al. (2012) showed many flat-bottomed lakes through the extensive
280 bathymetry surveys across the ACP of Alaska using a GPS-enabled sonar from a boat.

281 Additionally, as hydrology also affects the lake water level, the apparent lake bathymetry or lake
282 water depth, $h(x, y)$ must be adjusted by the water loss (or gain) per unit area. Therefore,

$$283 \quad h(x, y) = [1 - r_{deg}] \varphi(x, y) - H_{loss} , \quad (25)$$

284 where H_{loss} (m) is the elevation difference between the current water surface and original ground
285 surface before lake formation. At the lake center,

$$286 \quad H = [1 - r_{deg}]D - H_{loss} \quad . \quad (26)$$

287 Thus, the thermokarst lake bathymetry is affected by the ice-rich layer thickness, interannual
288 water balance, lake age, and talik geometry.

289 **3. Case study**

290 **3.1 Study area**

291 Peatball Lake (70°42.40N, 153°55.50W; 3 m above sea level) on the ACP of Alaska was chosen
292 for the demonstrative model application in this study as it has been relatively well documented in
293 previous studies (Lenz et al. 2016; Creighton et al., 2018; Parsekian et al., 2019). Figure 3 shows
294 the location of Peatball Lake within the Teshekpuk Lake subregion, as well as other subregions
295 that will be discussed later.

296 Peatball Lake, named for the abundant submerged peat balls on the lake bed, is a subcircular lake
297 on the Outer Coastal Plain of Alaska with a surface area of 1.18 km². Permafrost in this area is as
298 thick as ~400 m (Jorgenson et al., 2008), and the average volumetric ground ice content is about
299 77% in the near surface to a depth of 4 m (Kanevskiy et al., 2013). A talik has formed under
300 Peatball Lake because the maximum water depth of 2.5 m exceeds the maximum winter ice
301 thickness of 1.5 to 2.0 m (Arp et al., 2015; Lenz et al., 2016). The talik depth was estimated as
302 91 m at the lake center based on noninvasive TEM measurements (Creighton et al., 2018).
303 However, the talik may not be present beneath the shallow sublittoral shelves on the western
304 shore determined from the bathymetry (Lenz et al., 2016). Additionally, Lenz et al. (2016)

305 reported that, based on remote sensing imagery, Peatball Lake has expanded laterally between
306 0.02 and 1.36 m/year from 1955 to 2002.

307 **3.2 Geophysical survey of talik**

308 Geophysical field methods are effective for identifying and visualizing the frozen-unfrozen
309 interface, which is a key feature in permafrost dynamics (e.g., Pilon et al., 1985; Doolittle et al.,
310 1990; O'Neill et al., 2020; Rangel et al., 2021). For sub-lake taliks in the continuous permafrost
311 zone, Schwamborn et al. (2000) analyzed the sedimentary history of Lake Nikolay in the western
312 Lena River Delta using seismic reflection and ground penetrating radar (GPR). Other
313 geophysical methods such as surface nuclear magnetic resonance (NMR) can be used to detect
314 lake taliks (Parsekian et al., 2019) and remnant taliks in drained lake basins (Rangel et al., 2021).
315 At Peatball Lake, Creighton et al. (2018) estimated the talik depth using transient
316 electromagnetic (TEM) surveys along transects perpendicular to lakeshores. The dataset at
317 Peatball Lake is, to our knowledge, the only quasi-3D talik model available under an isolated
318 lake in the continuous permafrost zone because others are mostly sporadic talik depth
319 measurements at single drill points.

320 We applied the derived 3D Stefan equation to Peatball Lake based on 27 talik thickness point
321 measurements across the lake (Figure 4), estimated using TEM soundings (Creighton et al.,
322 2018) during spring 2016 and 2017. Figure 4 shows the observed talik thicknesses by the TEM
323 sounding (dots) and the fitted theoretical talik thickness estimates (contour lines) superimposed
324 over the corresponding lake bathymetry measured by Lenz et al. (2016).

325 The geometric parameters of the semi-ellipsoid model such as the talik center depth (D), the
326 cross-sectional aspect ratios (α_x & α_y), lake orientation azimuth angle and the lake center

327 location were systematically determined by grid searching to minimize the root mean square
328 difference (RMSD) between the model and thaw front obtained from the TEM data. The
329 optimum parameters for the smallest RMSD (5.94 m) are shown in Figure 4. Unexpectedly, the
330 basin orientation angle was found to be 23 degrees east from true north, unlike the orientation of
331 other surrounding lakes in the region. Comparison between the extrapolated talik geometry and
332 the lake bathymetry (Lenz et al., 2016) suggests the possibility of coalescence of two basins in
333 the past; a relatively common occurrence on the ACP of Alaska. However, if we had more TEM
334 measurement points, particularly in the “possible talik sub-basin”, the fitted talik geometry could
335 be different as the model was only fitted for the 27 TEM soundings. Despite irregularity due to
336 the complex lake formation history, the overall sub-lake talik geometry may be approximated by
337 a semi-ellipsoidal shape as indicated by the very good fit of the elliptic model to the TEM
338 measured talik thicknesses (see Figure 4 with overall RMSD = 5.94 m, 6.7 % of the maximum
339 talik depth). The idealized, thermally optimum model geometry can partition talik irregularity
340 associated with multi-generation lakes such as Peatball Lake.

341 Additionally, the gaps between the shoreline and the modeled talik extent located along north
342 and east shores occur where lake expansion is most rapid (Lenz et al., 2016). It has been
343 reported that thaw lake banks continuously retreat through a combination of thermal and
344 mechanical processes, although there is significant variability in rate of bank retreat depending
345 on region (Hopkins, 1949; Hopkins et al., 1955; Tomirdiaro, 1982; Rampton, 1982; Burn and
346 Smith, 1990; Jones et al. 2011, Lenz et al., 2016). Cross-sectional numerical thermal models
347 demonstrated that the expansion rates are affected by the talik thickness (Plug and West, 2009)
348 and seasonal snow cover (Ling and Zhang, 2003a). The disagreement between the lake and talik

349 extents on the north and east shores of Peatball Lake implies that rapid horizontal lake expansion
350 can locally dominate permafrost thaw and subsidence processes even in a lake with a talik.

351 Figure 5 compares the observed lakebed and talik profiles in Peatball Lake along the north-south
352 center line and along transects (b) – (c), respectively. Note that the TEM transects for the talik is
353 not a straight line (See Figure 4); therefore, the fitted theoretical line shows irregularity. Figure
354 5A illustrates that the lakebed profile is characterized by flatter trapezoidal geometry compared
355 to the elliptic talik. In fact, there is a clear inflection in the linear regression line at a talik depth
356 of ~50 m in Figure 5B. From the slopes of the regression lines, the permafrost degradation rates
357 r_{deg} are computed as 97.3 % and 99.7 % for the shallow talik section (50 m or less) and the deep
358 section (50 m or more), respectively. This analysis suggests that the subsidence due to
359 permafrost thaw continues even after the shallow ice-rich part of the permafrost (about 4 meters,
360 Kanevskiy, 2013) is thawed while it has diminished around the depth of 50 meter under Peatball
361 Lake. This case study demonstrates a link between lake bathymetry and talik thickness
362 associated with a layered permafrost structure.

363 **3.3 Depth-width ratio and temperature gradient**

364 The analysis (Equations 22 & 23) suggests the proportional relationship between lake/talik
365 geometry and thaw energy. That is,

$$366 \quad a: b: D = \alpha_x: \alpha_y: 1 = \xi: \eta: \zeta = q_{f,x}: q_{f,y}: q_{f,z} \quad . \quad (27)$$

367 Combining Equations (27), (1) and (4), the depth-width (radius) ratio of the talik may be written
368 as follows:

$$369 \quad a: D = \left(q_{in,x} + k_p \frac{dT}{dr} \right) : \left(q_{in,z} + k_p \frac{dT}{dn} \right) \quad (28)$$

370 where r and n are the horizontal and vertical distances from the original permafrost surface
 371 center, respectively, and a is the representative horizontal radius of the lake. This expression
 372 states that the anisotropic top-down permafrost thaw is caused by anisotropy of the thermal
 373 gradient for uniform incoming energy and uniform thermal properties of near surface
 374 permafrost. For example, since the vertical thermal gradient is typically steeper than the
 375 horizontal gradient during the critical summer months (Carson and Hussey, 1962; illustration in
 376 Figure 1), the heat energy in the vertical direction is used more for heat conduction rather than
 377 permafrost thawing. The vertical temperature gradient is always negative near the talik
 378 boundary in the permafrost ($\frac{dT}{dn} < 0$) at the center of the lake while the inter-seasonal average
 379 of the horizontal thermal gradient may be negligible ($\frac{dT}{dr} \approx 0$). As a result, lateral thaw is faster
 380 than vertical thaw due to less energy loss to horizontal heat conduction (McClymont et al.,
 381 2013; Devoie et al., 2021). Assuming the normal heat flux to the phase boundary is uniform
 382 throughout the phase boundary surface ($q_{in,x} = q_{in,z} = q_{in}$), Equation (28) can be simplified as
 383 follows:

$$384 \quad \frac{D}{a} = 1 + \frac{k_p}{q_{in}} \frac{dT}{dn} \quad , \text{ or } \quad q_{in} = -\frac{ak_p}{a-D} \frac{dT}{dn} \quad . \quad (29)$$

385 This simple expression may be a useful tool to link the lake depth-width ratio, the lake average
 386 heat flux q_{in} , and the vertical temperature gradient $\frac{dT}{dn}$ at the base of the talik. Since $\frac{dT}{dn} < 0$ in
 387 the permafrost near the talik boundary, the D/a is always less than 1 (flatter than a semi-sphere).
 388 However, the depth-width ratio of the talik depends on the vertical temperature slope near the
 389 talik boundary, which is likely affected by talik age. For instance, Mackay's analytical model
 390 (1962) suggests that the vertical temperature gradient below the lake center begins steeply at the

391 talik initiation, and then over time it approaches a lower slope at equilibrium. Therefore, the
392 formula in Equation (29) suggests that a younger talik should be flatter while an older talik
393 approaches a deeper semi-spheric shape ($D/a \rightarrow 1$).

394 Table 1 shows the estimated incoming heat flux with the key parameters using the proposed
395 formula (Equation (29)). Creighton et al. (2018) applied the CRYOGRID2 model (Westerman et
396 al., 2013) to Peatball Lake. The temperature slope at the talik bottom at the lake center was
397 estimated by the Mackay's analytical model assuming the lake age of 1400 years since the talik
398 initiation with the same model configuration Creighton et al. (2018) adopted. Creighton et al.
399 (2018) estimated the interannual mean heat flux q_{in} to be 0.070 (W/m²), which is very close to
400 our estimate. As this simplified formula is consistent with the well-configured modeling result,
401 the horizontal thermal gradient contribution to the vertical aspect ratio of the talik seems to be
402 very small in Peatball Lake.

403 Moreover, this relationship may be useful to incorporate the three-dimensional talik expansion
404 effect in a simple analysis without fully integrated permafrost thermal modeling. For example, if
405 the mean energy flux increases 10 percent from current climate conditions (e.g., shorter lake
406 freeze period), assuming all other properties and horizontal thermal gradient variation remain
407 unchanged, the talik depth-width ratio D/a would shift from 0.171 to 0.234 toward the new
408 equilibrium state. Therefore, this analysis suggests that a warmer climate may promote
409 permafrost thaw in the vertical direction more than in the horizontal direction. Hence, it is
410 important to quantify the vertical thawing as well as the visible lake horizontal expansion in
411 order to evaluate the impact of the climate change on permafrost thaw beneath thermokarst lakes.

412 **4. Discussion**

413 **4.1 Relationship between hypothetical models**

414 To illustrate the applicability of the thermal model presented here, the available hypothetical
415 models of thermokarst lake growth are compiled in Figure 6. This diagram focuses on the
416 physical processes after the lake initiation stage assuming the bio-ecological effects are
417 negligible.

418 Figure 6 illustrates the evolution of the talik in ice-rich permafrost over time, with driving
419 processes shown in the right panel. In Stage A, the mechanical processes of wave erosion and
420 thaw slumping along lake margins dominate lake expansion in summer, and shallow water favors
421 grounded lake ice in the winter. In time (Stage B), the lake deepens from thaw subsidence
422 beneath the older lake center. Winter ice may freeze to the lake bed, but heat loss is insufficient
423 to freeze the underlying thawed lake bed sediments. A shallow talik develops as thermal
424 processes work in tandem with mechanical processes, the latter now enhanced by more vigorous
425 lake circulation. By Stage C, the talik is well developed beneath the entire lake basin as ground
426 subsidence continues. Eventually (Stage D), the winter ice cover no longer extends to the lake
427 bed, but instead floats atop a residual pool of lake water, while milder vertical temperature
428 gradient beneath the lake deepens the talik as the lake matures. Thermomechanical erosion of
429 lake margins, especially if there are prominent banks in hilly terrain, promotes sedimentation on
430 near-shore shelves, and the underlying talik may begin refreezing. If the lake hasn't drained by
431 this point (Stage E), the talik beneath the lake center extends deeper into the permafrost although
432 subsidence may cease as the excess ice content diminishes with depth. Where many large, old

433 lakes exist, the permafrost may be riddled with deep taliks, and some may eventually penetrate to
434 the permafrost base to create an open talik.

435 Talik development is affected by climatic and local conditions that favor talik initiation and
436 growth including:

- 437 • Deepening lake waters triggered by greater precipitation and/or reduced evaporation,
438 which promotes a floating ice regime
- 439 • Presence of ice-rich sediments (e.g., Yedoma) beneath lakes
- 440 • Warmer lake water induced by regional warming or by longer ice-free summers
- 441 • Thinner winter ice cover due to warmer winter temperatures and/or deeper snow

442 Conversely, talik growth cessation or contraction can occur when the same drivers are reversed,
443 if the lake partially or completely drains, or when the lake basin is filled with sediments. The
444 latter scenario is more likely in hilly terrain when the expanding lake erodes high banks and lake
445 currents redistribute sediments.

446 **4.2 Thermal process and preferential expansion**

447 **4.2.1 Lake geometry and heat balance**

448 The analytical expression of the lake geometry may be useful to analyze horizontally oriented
449 lakes with direction dependent elongation as well. From Equation (27) and (1), we have,

$$450 \quad a: b = q_{f,x}:q_{f,y} = (q_{in,x} - q_{c,x}): (q_{in,y} - q_{c,y}), \quad (30)$$

451 where a and b are the semi-major and -minor axes of the elongated lake, respectively. When
 452 horizontal heat conduction into the tundra is negligible, ($q_{c,r} = k_p \frac{dT}{dr} \approx 0$), this equation can be
 453 reduced to,

$$454 \quad a: b = q_{in,x}: q_{in,y}. \quad (31)$$

455 Hence, the aspect ratio of elliptic lakes can be explained by heat supply inequality if the lake
 456 geomorphology process is dominated by thermal process. As expressed in Equation (3), there are
 457 two different components in the incoming heat flux to the lake banks: surface energy flux and
 458 heat conduction from the lake water body. Thus, the lake aspect ratio may be written as,

$$459 \quad a: b = \left(q_{suf,x} - k_L \frac{dT}{dx} \right) : \left(q_{suf,y} - k_L \frac{dT}{dy} \right) \quad (32)$$

460 **4.2.2 Incoming radiation imbalance effect**

461 One of the incoming surface energy flux inequalities q_{suf} may be caused by shortwave radiation
 462 along the lake shoreline. The daily potential solar irradiation on a sloping surface can be
 463 computed by the trigonometric function (e.g., Equation B.11 in DeWalle and Rango, 2008). The
 464 total daily radiation is a function of latitude and bank slope angle, which depends on the
 465 permafrost degradation rate, the maturity of the talik, and ground ice distribution.

466 Figure 7 shows the computed mean daily potential solar irradiation on the sloping lakeshore (I'_q)
 467 relative to a flat surface (I_q) during the summer period (June-August) at three different latitudes.
 468 The shape of this diagram may correspond to the shape of a thermokarst lake as the enhanced
 469 radiation results in more permafrost thaw. The difference in relative incoming radiation will
 470 diminish as bank slope angle lessens. In general, the south facing slope along the northern shore

471 tends to receive more radiation than the north facing slope (e.g., Séjourné et al., 2015). This
472 tendency is more pronounced in lower latitude zones due to the higher mid-day sun angle.
473 It is interesting that at 65 and 60 degree latitude the north and south facing banks receive slightly
474 less radiation than east and west facing slopes, while an opposite result occurs at 70 degree
475 latitude (Figure 7). Therefore, the radiation imbalance may partially explain the north-south
476 elongation along the 70 degree latitude line and the west-east elongation of lower latitude (60-65
477 degrees) of lowland thermokarst lakes shown by Grosse et al. (2013, Figure 19). However,
478 because these small differences in incoming radiation imbalance alone are insufficient to result
479 in the distinctive lake elongation in the ACP, they likely introduce rather minor additional
480 complexities in lake spatial shape.

481 **4.3 Wind wave erosion and preferential expansion**

482 Wind wave erosion plays an important role in horizontal expansion of shallow lakes because
483 waves can undercut the vegetated bank (Hopkins, 1949). Wind waves make the water bodies
484 (e.g., lakes and bays) round by local net sediment flux even in low latitude regions (e.g., Ashton
485 et al., 2009). The effect of waves on shoreline morphology has been analyzed in the coastal
486 engineering field: for example, Silvester (1974) investigated the equilibrium shape of bays under
487 different wave conditions using laboratory wave experiments and found that the stable beach in
488 the bay adapted a half-heart or cardioid shape for a fixed wave direction in the absence of
489 sediment supply. Reeve et al. (2018) showed theoretically that the equilibrium coastline shape
490 can be expressed as a diffusion type equation through incorporating the wave diffraction effect,
491 which makes the wave crest line nearly parallel to the shore. However, according to the shallow
492 water wave theory, which is applicable for small fetch distances on lakes in the ACP, water

493 waves do not cause any sediment transport without current, although wave motion is a key factor
494 for the mobilization of the sediment (e.g., Carson and Hussey, 1962).

495 Wind-induced water circulation in a shallow, oval lake was perhaps first analyzed by
496 Livingstone (1954) who showed theoretically that the current around the lake ends may be
497 accelerated efficiently by wind-induced return rip currents. However, the lake water circulation
498 pattern assumed in his study (shown in the left side of Figure 8) was less common than the
499 pattern described by Carson and Hussey (1962), who observed reverse circulation patterns near
500 the lake ends, as shown in the right side of Figure 8. For convenience, we refer to two distinctive
501 current patterns: the Livingstone type and the Carson & Hussey (C&H) type. C&H type
502 circulation can indeed explain the commonly observed peat and sediment bars near the leeward
503 lake side shores. Carson and Hussey (1962) noted that sedimentation on the leeward lake side
504 can provide protection from mechanical wave erosion as well as insulation from permafrost
505 thaw, which result in lake elongation. They also observed that preferential bank erosion is
506 typically focused in zones oriented 50 degrees to wave approach. The return flow was found to
507 concentrate around the windward lake side, which accelerates the mechanical erosion and
508 sediment transport at the lake ends. However, the Livingstone type circulation might occur
509 depending on the local wind field as it can explain the sublittoral shelf formation on the
510 windward shore. In either case, the wind-induced current effect on lake elongation can be
511 supported by Livingstone's theory (1954) which should be valid for both circulation types. Thus,
512 the combination of wind wave mobilization and lake water circulation is the most accepted
513 hypothesis for lake elongation during the relatively young shallow lake expansion stage (Carson,
514 1968; Arp et al., 2011, Hinkel et al., 2012).

515 The shallow wave theory states that the sediment mobilization due to wind wave only occurs in
516 shallow water (wave height >4 % of water depth, e.g., Reeve et al., 2018). Therefore, the
517 contribution of the wind wave effect to lake elongation may be reduced as the lake deepens.
518 Figure 9 shows a plot of lake length:width ratios versus the percent of lakes with a bedfast ice
519 regime in seven study regions in Alaska determined with satellite-based synthetic aperture radar
520 imagery (Engram et al., 2018). The study regions represent differences in permafrost
521 characteristics and climate that appear to be reflected in this comparison of length:width ratio
522 and the percent of lakes in a region that freeze to their bed and thus likely do not have a sub-lake
523 talik. For example, lakes in the Teshekpuk Lake and Kuparuk study areas have a shape that is
524 nearly twice as long as it is wide. In both of these regions, more than 80% of the lakes freeze to
525 their bed and likely do not have a talik. This is contrast to lakes located near Umiat and on the
526 Seward Peninsula, that have primarily developed in Yedoma permafrost deposits. Lakes near
527 Umiat and on the Seward Peninsula tend to be more circular ($L:W = 1.3$ to 1.4) and more than
528 90% likely have a talik since they do not freeze to their bed in the winter. The differences
529 observed here relative to elongation of lakes and whether the region primarily has lakes that
530 freeze to their bed or not likely demonstrates a key aspect related to the role of wind-wave
531 erosion. In general, the shallower lakes common in coastal areas, such as Teshekpuk, Barrow,
532 and Kuparuk, are more elongated likely due to wind wave erosion. Whereas lakes in Umiat (ice-
533 rich permafrost), Seward Peninsula (ice-rich permafrost), and Inigok (ice-poor permafrost) tend
534 to be rounder because of talik development and the presence of deeper lakes (on the order of 10-
535 20 m in some instances). This remote-sensing based evidence implies that the wind effect seems
536 to be limited by the lake thermal subsidence due to sub-lake talik development, while shallow
537 lakes with the bedfast ice may continue elongating by wind erosion.

538 **4.4 Applicability of the 3D Stefan equation**

539 The limitations of the derived 3D Stefan Equation (Equation 22) are summarized in this section
540 along with Figure 6. Once a seasonal pond is formed on the permafrost, it primarily expands
541 horizontally by wind wave erosion and the thaw slump process (Livingstone, 1954; Carson &
542 Hussey, 1962; Rex, 1961; Hinkel et al., 2012, Grosse et al., 2013) because the active layer
543 beneath the pond likely freezes every year. On the flat ACP of Alaska, lake thaw slumps tend to
544 be the result of topography (e.g., slope and aspect of the ground surface) while lake elongation is
545 likely caused by wind wave erosion. As described above, preferential bank thaw at the lake ends
546 can be explained by the insulation effect of the sediments carried by the water current (likely, the
547 C&H type circulation) because the sublittoral shelf may be initiated at this stage.

548 When seasonal thawing penetrates more deeply than the annual freezing depth, a talik may be
549 initiated, typically around the deepest point near the center of the lake (Lachenbruch et al. 1962).
550 Sellmann (1975) described this process, which is one of the mechanisms for shelf formation in a
551 thermokarst lake. For the horizontal expansion stage, A in Figure 6, the proposed quasi-steady
552 state thermal model may not be appropriate because the lakeshore expansion imbalance occurs at
553 least minimally throughout the lake expansion process. However, the 3D Stefan equation may
554 be able to characterize the talik in the initiation stage B in Figure 6.

555 Once the talik is established, the 3D Stefan's thermal model proposed here suggests that the talik
556 may begin to influence lake geometry. Since sediment mobilization due to wind-driven waves
557 occurs in shallow water, lake elongation by waves may diminish as the lake deepens via ground
558 subsidence (Figure 9). Lake water effectively collects energy from the surface during summer
559 and the talik stores the excess heat throughout the winter. Arp et al. (2010, 2011) and Jefferies et

560 al. (1999) discussed the difference in heat conduction between a grounded ice lake and a floating
561 ice lake. Their observations are generally consistent with the proposed theory because a deeper
562 talik under a floating ice lake should have a greater heat capacity. Since lake elongation likely
563 occurs before talik formation, the horizontal lake characterization derived in this study may not
564 be fully applicable to the analysis of thaw lakes on the ACP. In fact, the disagreement of the
565 talik and lake extents in Peatball Lake application illustrates the multiple effects on the lake
566 bathymetry and orientation. Clearly, however, talik expansion and concurrent subsidence
567 stabilizes lake geometry and contributes to lake roundness.

568 The applicability of the proposed 3D Stefan equation is limited for lakes with high sediment
569 influx and for lakes with through talik. The paired sublittoral shelves on both lake sides are
570 commonly found in the sand dune areas of the southern ACP. The talik shape is likely altered by
571 uneven sediment deposition that affects the temperature gradient normal to the phase boundary
572 as mentioned by several researchers (Hunter et al., 1981; Mackay, 1992; West and Plug, 2008).
573 The shelves created by sediment redistribution due to lake water circulation adds complexity to
574 the ellipsoidal talik shape described in this study. Finally, if the talik penetrates through the
575 permafrost and becomes a throughgoing talik (Hinkel and Arp, 2015), the proposed thermal
576 theory herein is no longer applicable for thermokarst lake and talik characterization.

577 Lastly, the 3D Stefan equation assumes fully saturated talik and isotropic thermal properties.
578 However, uneven consolidation of thawed porous media and layered structure of the permafrost
579 may cause anisotropic thermal conductivities. When the effect of direction dependency in the
580 thermal conductivity is found to be significant, it can be incorporated into the formulation of the
581 anisotropic heat conduction into the permafrost.

582 **5. Conclusions**

583 The theory presented here addresses the origin of the thermokarst lake ellipticity on the ACP.

584 Elliptic lake geometry results from minimizing overall thawing energy consumption for a given
585 incoming energy load. This is particularly applicable for mature, deep thermokarst lakes with
586 well-developed taliks. Additionally, existing hypothetical models were reviewed to illuminate
587 the thermal effect (e.g., ellipsoidal talik geometry) on the thermokarst lake morphology.

588 The derived ellipsoid talik model integrates the atmospheric forcing (or incoming energy), the
589 vertical thermal gradient, the thermal diffusivity of the permafrost, and the talik geometry. Heat
590 flux by conduction into the permafrost depends on the heat gradient of the underlying permafrost
591 (Fourier's law). As the vertical temperature slope diminishes with talik maturation, the depth-
592 width ratio of the talik becomes larger creating a deeper talik; thus, much of incoming energy is
593 likely consumed for vertical rather than horizontal expansion. Conversely, during the early
594 stages, thermo-mechanical processes such as wind-driven wave erosion dominates horizontal
595 expansion and elongation of the lake. Consequently, this theory elucidates how talik expansion
596 and concurrent permafrost degradation stabilizes the shape of thermokarst lake to one that is
597 more round rather than elliptical.

598 The semi-ellipsoidal 3D Stefan equation is, to our knowledge, the first geometric model
599 explicitly derived only from the energy conservation equation at the phase boundary. The vector
600 form of the energy conservation equation (Equation 5) in a 3D anisotropic thermal field was
601 integrated at the phase boundary area under the isolated general-shaped lake to quantify the total
602 energy balance. It was shown that the basin total thaw energy or talik expansion rate is
603 equivalent to the weighted phase boundary area. The optimum talik shape function was

604 determined by the variational principle as an extremum of the functional that minimizes the total
605 thawing energy consumption (the stationary action principle). Thus, the resultant semi-ellipsoid
606 equation (Equation 22) can be considered the 3D Stefan equation because it describes the
607 optimum geometry of phase boundary.

608 The derived semi-ellipsoid function was applied to Peatball Lake, ACP of Alaska, where the
609 talik was extensively surveyed using TEM soundings. The pure geometric fitting exercise met
610 the 27 measured TEM data point well with RMSD of 5.94 m, although the talik orientation
611 disagreed with orientation of Peatball Lake and other surrounding lakes. This may be induced by
612 the irregularity due to the rapid and uneven horizontal lake expansion, or possibly by basin
613 coalescence. Comparing the observed talik thickness to the observed lake bathymetry indicated
614 two distinctive permafrost degradation scenarios: significant subsidence by near-surface ice-rich
615 layer thaw and minor contribution of subsidence due to ice-poor permafrost thaw at depth.
616 Consequently, lake water depth is affected by uneven subsidence of thawing permafrost, the
617 interannual water balance; the spatial lake shape irregularity was determined during earlier stage
618 of development. Therefore, careful consideration is required for the analysis of the relationship
619 between lake bathymetry and talik thickness. Nevertheless, this theoretical technique can be
620 used as guidance to partition various effects such as talik development and thaw subsidence,
621 wind wave erosion, lake ice thickness, surficial geology type, and sediment transport by lake
622 water current. Moreover, the analytical expression of the 3D Stefan Equation can be potentially
623 incorporated in the global or regional scale Earth system model to describe missing sub-grid
624 scale processes such as lake dynamics with minimal additional computational resources.

625 **Appendix A: Alternative derivation using isoperimetric inequality**

626 Alternative derivation may provide the thermally optimum talik shape minimizing the phase
 627 boundary area A with a fixed talik volume V . Equation (14) establishes talik volume and phase
 628 boundary area under the thermokarst lake by a general function of the phase boundary φ . The
 629 horizontal coordinate system may be transformed by $(u, v) = \left(\frac{x}{\alpha_x}, \frac{y}{\alpha_y}\right)$. Then, the phase
 630 boundary can be expressed as a scaled function,

631
$$\hat{\varphi}(u, v) = \varphi(x, y) = \varphi(\alpha_x u, \alpha_y v), \quad (u, v) \in \hat{B}. \quad (\text{A1})$$

632 According to,

633
$$\begin{cases} \frac{du}{dx} = \frac{1}{\alpha_x}, \\ \frac{dv}{dy} = \frac{1}{\alpha_y}, \\ \frac{\partial}{\partial u} \hat{\varphi}(u, v) = \frac{\partial}{\partial u} \varphi(\alpha_x u, \alpha_y v) = \alpha_x \varphi_x, \\ \frac{\partial}{\partial v} \hat{\varphi}(u, v) = \frac{\partial}{\partial v} \varphi(\alpha_x u, \alpha_y v) = \alpha_y \varphi_y \end{cases} \quad (\text{A2})$$

634 the talik volume and the phase boundary area can be written as,

635
$$\begin{cases} V[\varphi] = \alpha_x \alpha_y \iint_{\hat{B}} \hat{\varphi} \, dudv \\ A[\varphi] = \alpha_x \alpha_y \iint_{\hat{B}} \sqrt{\hat{\varphi}_u^2 + \hat{\varphi}_v^2 + 1} \, dudv = \alpha_x \alpha_y \int_{\hat{S}} d\hat{S} \end{cases}, \quad (\text{A3})$$

636 where \hat{B} denotes the extent of $\hat{\varphi}(u, v)$ on the uv plane, and \hat{S} is the surface on $z = \hat{\varphi}(u, v)$ as,

637
$$\hat{S} = \{ (u, v, z) \in \mathbb{R}^3 \mid (u, v) \in \hat{B}, z = \hat{\varphi}(u, v) \}. \quad (\text{A4})$$

638 The horizontal scaling transform makes it a symmetric closed surface on $z = 0$,

639
$$S^* = \{ (u, v, z) \in \mathbb{R}^3 \mid (u, v) \in \hat{B}, z = \pm \hat{\varphi}(u, v) \}. \quad (\text{A5})$$

640 It is known that volume U enclosed by the ovaloid surface S^* and its surface area satisfy the
 641 isoperimetric inequality for an ovaloid surface, which can be written as,

$$642 \quad \left(\int_{S^*} dS^* \right)^3 \geq 36\pi U^2 . \quad (\text{A6})$$

643 As the volume and the surface area of the convex closed surface S^* can be expressed as

$$644 \quad U = 2 \left| \iint_{\hat{B}} \hat{\varphi} \, dudv \right| = \frac{2}{\alpha_x \alpha_y} |V[\varphi]| , \text{ and} \quad (\text{A7})$$

$$645 \quad \int_{S^*} dS^* = 2 \int_{\hat{S}} d\hat{S} = \frac{2}{\alpha_x \alpha_y} A[\varphi] , \text{ respectively,} \quad (\text{A8})$$

646 we have,

$$647 \quad \left(\frac{2}{\alpha_x \alpha_y} A[\varphi] \right)^3 \geq 36\pi \left(\frac{2}{\alpha_x \alpha_y} V[\varphi] \right)^2 , \text{ or}$$

$$648 \quad A[\varphi] \geq \sqrt[3]{18\pi \alpha_x \alpha_y (V[\varphi])^2} . \quad (\text{A9})$$

649 The equality in Equation (A9) holds only if the surface S^* is a sphere, which maximizes the
 650 volume. Let the radius of this sphere,

$$651 \quad D = \sqrt[3]{\frac{3}{4\pi} V} = \sqrt[3]{\frac{3|A[\varphi]|}{2\pi \alpha_x \alpha_y}} . \quad (\text{A10})$$

652 From the symmetricity to the plane $z = 0$, we can obtain,

$$653 \quad \hat{\varphi}(u, v) = -D \sqrt{1 - \left(\frac{u}{D}\right)^2 - \left(\frac{v}{D}\right)^2} , \quad (u, v) \in \hat{B} . \quad (\text{A11})$$

654 Inverse scaling coordinate transformation yields the ellipsoid phase boundary function as
 655 follows:

656
$$\varphi(x, y) = -D \sqrt{1 - \left(\frac{x}{\alpha_x D}\right)^2 - \left(\frac{y}{\alpha_y D}\right)^2}, \quad (x, y) \in B, \quad (\text{A12})$$

657 where D is the depth of the talik at the center. The ellipsoid, the three-dimensional Stefan
 658 Equation for talik, can be obtained by the isoperimetric inequality as well as the functional
 659 analysis.

660 **Appendix B: Determination of the coefficients d and λ**

661 We can determine two coefficients in the ellipsoid (Equation 21) by further application of the
 662 variational principle. Let

663
$$D = \frac{2}{|\lambda|}. \quad (\text{B1})$$

664 Also, let the intersect d proportional to the vertical radius of the ellipsoid, as follows:

665
$$d = tD \quad (-1 \leq t < 1), \quad (\text{B2})$$

666 where t is a parameter describing the relative elevation of the basin to the original ground
 667 surface. Then, Equations (20) and (21) can be rewritten as,

668
$$z = -\varphi = -\sqrt{D^2 - \frac{x^2}{\alpha_x^2} - \frac{y^2}{\alpha_y^2}} + tD, \quad \text{and} \quad (\text{B3})$$

669
$$\left(\frac{x}{\alpha_x D}\right)^2 + \left(\frac{y}{\alpha_y D}\right)^2 + \left(\frac{z-tD}{D}\right)^2 = 1, \quad \text{respectively.} \quad (\text{B4})$$

670 Now, the phase boundary area and volume can be evaluated as functions of the parameter t :

671

$$\begin{aligned}
V[\varphi] &= \iint_B \varphi \, dx dy = \iint_B \left(-\sqrt{D^2 - \frac{x^2}{\alpha_x^2} - \frac{y^2}{\alpha_y^2}} + tD \right) \, dx dy \\
&= \pi \alpha_x \alpha_y \int_{-(1-t)D}^0 \{D^2 - (tD - z)^2\} dz \\
&= \frac{\pi}{3} \alpha_x \alpha_y D^3 (t^3 - 3t + 2)
\end{aligned}
\tag{B5}$$

672

$$\begin{aligned}
A[\varphi] &= \iint_B \sqrt{\alpha_x^2 \varphi_x^2 + \alpha_y^2 \varphi_y^2 + 1} \, dx dy \\
&= \iint_B \frac{1}{\sqrt{1 - \left(\frac{x}{\alpha_x D}\right)^2 - \left(\frac{y}{\alpha_y D}\right)^2}} \, dx dy \\
&= \pi \alpha_x \alpha_y D^2 \left\{ (1 - t^2) + \int_1^{\frac{1}{z^2}} \left(\frac{1}{z^2} - t^2 \right) dz \right\} \\
&= 2\pi \alpha_x \alpha_y D^2 (1 - t)
\end{aligned}
\tag{B6}$$

673 Eliminating D from these expressions yields,

674

$$A[\varphi]^3 = M \frac{(1-t)^3}{(t^3 - 3t + 2)^2} \tag{B7}$$

675 where M is a positive constant. Therefore, as

676

$$\frac{d}{dt} (A[\varphi]^3) = M \frac{3t}{(1-t)^2 (t+2)^3} > 0 \quad (-1 \leq t < 1), \tag{B8}$$

677 the phase boundary area $A[\varphi]$ is the minimum at $t = 0$. Hence, $d = 0$ that corresponds to a semi-
678 ellipsoid with depth D at the center.

679 **Author contribution**

680 Ohara and Yamatani developed the theory, and all other co-authors, especially Hinkel, Jones,
681 Parsekian, and Kanevskiy, offered crucial advice in interpretation. Jones and Parsekian provided
682 the field observed data for the case study of Peatball Lake. Jones performed the statistical
683 analysis on the oriented lakes based on SAR-satellite remote-sensing data. Ohara prepared the
684 manuscript with contributions from all co-authors.

685 **Acknowledgements**

686 This study was supported by the National Science Foundation (NSF) under awards OPP-
687 1806287, 1806213, and 1806202. The authors thank UIC Science and CH2MHill Polar Field
688 Services (now Battelle Arctic Research Operations) for logistical field support. Datasets and
689 sources code for this research are available in these in-text data citation references. Louise
690 Farquharson and Benjamin Gaglioti provided helpful comments improving the manuscript.

691 **References**

- 692 Arp, C. D., Jones, B. M., Schmutz, J. A., Urban, F. E., & Jorgenson, M. T.: Two mechanisms of
693 aquatic and terrestrial habitat change along an Alaskan Arctic coastline, *Polar Biology*,
694 33(12), 1629-1640, 2010.
- 695 Arp, C. D., Jones, B. M., Urban, F. E., & Grosse, G.: Hydrogeomorphic processes of thermokarst
696 lakes with grounded - ice and floating - ice regimes on the Arctic coastal plain,
697 Alaska, *Hydrological Processes*, 25(15), 2422-2438, 2011.
- 698 Arp, C. D., Whitman, M. S., Jones, B. M., Kemnitz, R., Grosse, G., & Urban, F. E.: Drainage
699 network structure and hydrologic behavior of three lake-rich watersheds on the Arctic
700 Coastal Plain, Alaska. *Arctic, Antarctic, and Alpine Research*, 44(4), 385-398, 2012.
- 701 Arp, C. D., Jones, B. M., Liljedahl, A. K., Hinkel, K. M., & Welker, J. A.: Depth, ice thickness,
702 and ice - out timing cause divergent hydrologic responses among Arctic lakes. *Water*
703 *Resources Research*, 51(12), 9379-9401, 2015.

704 Arp, C. D., Jones, B. M., Grosse, G., Bondurant, A. C., Romanovsky, V. E., Hinkel, K. M., &
705 Parsekian, A. D.: Threshold sensitivity of shallow Arctic lakes and sublake permafrost to
706 changing winter climate, *Geophysical Research Letters*, 43(12), 6358-6365, 2016.

707 Ashton, A.D., Murray, A.B., Littlewood, R., Lewis, D.A. and Hong, P.: Fetch-limited self-
708 organization of elongate water bodies, *Geology*, 37(2), pp.187-190, 2009.

709 Black, R. F., & Barksdale, W. L.: Oriented lakes of northern Alaska, *The Journal of Geology*,
710 57(2), 105-118, 1949.

711 Brewer, M. C.: The thermal regime of an arctic lake, *Eos, Transactions American Geophysical*
712 *Union*, 39(2), 278-284, 1958.

713 Burn, C. R., & Smith, M. W.: Development of thermokarst lakes during the Holocene at sites
714 near Mayo, Yukon Territory, *Permafrost and Periglacial Processes*, 1(2), 161-175, 1990.

715 Burn, C.R.: Tundra lakes and permafrost, Richards Island, western Arctic coast, Canada,
716 *Canadian Journal of Earth Sciences*, 39(8), pp.1281-1298, 2002.

717 Carslaw, H. S., & Jaeger, J. C.: *Conduction of heat in solids*. Oxford: Clarendon Press, 1959.

718 Carson, C. E.: Radiocarbon dating of lacustrine strands in Arctic Alaska. *Arctic*, 12-26, 1968.

719 Carson, C. E., & Hussey, K. M.: The oriented lakes of Arctic Alaska, *The Journal of Geology*,
720 70(4), 417-439, 1962.

721 Carter, L. D.: A Pleistocene sand sea on the Alaskan Arctic coastal plain, *Science*, 211(4480),
722 381-383, 1981.

723 Cassel, K. W.: Variational methods with applications in science and engineering, Cambridge
724 University Press, 2013.

725 Courant, R., & Hilbert, D.: Methods of mathematical physics, *Bulletin of the American*
726 *Mathematical Society*, 60, 578-579, 1954.

727 Creighton, A. L., Parsekian, A. D., Angelopoulos, M., Jones, B. M., Bondurant, A., Engram,
728 M., ... & Arp, C. D.: Transient electromagnetic surveys for the determination of talik
729 depth and geometry beneath thermokarst lakes, *Journal of Geophysical Research: Solid*
730 *Earth*, 123(11), 9310-9323, 2018.

731 Czudek, T. and Demek, J.: Thermokarst in Siberia and its influence on the development of
732 lowland relief, *Quaternary Research*, 1(1), pp.103-120, 1970.

733 Devoie, É.G., Craig, J.R., Dominico, M., Carpino, O., Connon, R.F., Rudy, A.C. and Quinton,
734 W.L.: Mechanisms of Discontinuous Permafrost Thaw in Peatlands, *Journal of*
735 *Geophysical Research: Earth Surface*, 126(11), p.e2021JF006204, 2021.

736 DeWalle, D. R., & Rango, A.: Principles of snow hydrology, Cambridge University Press, 2008.

737 Doolittle, J. A., Hardisky, M. A., & Gross, M. F.: A ground-penetrating radar study of active
738 layer thicknesses in areas of moist sedge and wet sedge tundra near Bethel, Alaska, USA.
739 *Arctic and Alpine Research*, 22(2), 175-182, 1990.

740 Engram, M., Arp, C. D., Jones, B. M., Ajadi, O. A., & Meyer, F. J.: Analyzing floating and
741 bedfast lake ice regimes across Arctic Alaska using 25 years of space-borne SAR
742 imagery. *Remote sensing of environment*, 209, 660-676, 2018.

743 Farquharson, L., Anthony, K.W., Bigelow, N., Edwards, M. and Grosse, G.: Facies analysis of
744 yedoma thermokarst lakes on the northern Seward Peninsula, Alaska. *Sedimentary*
745 *Geology*, 340, pp.25-37, 2016.

746 French, H.M. 2018. *The Periglacial Environment*. 4th ed. John Wiley and Sons Ltd., Chichester,
747 UK, 515 pp.

748 Gelfand, I. M., & Fomin, S. V.: *Calculus of variations*. Revised English edition translated and
749 edited by Richard A. Silverman. *Prentice Hall, Englewood Cliffs, NJ*, 7, 10-11, 1963.

750 Grosse, G., Jones, B. M., & Arp, C. D.: Thermokarst lakes, drainage, and drained basins. In:
751 Shroder, J. (Editor in Chief), Giardino, R., Harbor, J. (Eds.), *Treatise on Geomorphology*.
752 Academic Press, San Diego, CA, vol. 8, *Glacial and Periglacial Geomorphology*, pp.
753 325–353, 2013.

754 Heslop, J.K., Walter Anthony, K.M., Sepulveda-Jauregui, A., Martinez-Cruz, K., Bondurant, A.,
755 Grosse, G. and Jones, M.C.: Thermokarst lake methanogenesis along a complete talik
756 profile, *Biogeosciences*, 12(14), pp.4317-4331, 2015.

757 Hinkel, K. M., Frohn, R. C., Nelson, F. E., Eisner, W. R., & Beck, R. A.: Morphometric and
758 spatial analysis of thaw lakes and drained thaw lake basins in the western Arctic Coastal
759 Plain, Alaska, *Permafrost and Periglacial Processes*, 16(4), 327-341, 2005.

760 Hinkel, K. M., Sheng, Y., Lenters, J. D., Lyons, E. A., Beck, R. A., Eisner, W. R., & Wang, J.:
761 Thermokarst lakes on the Arctic coastal plain of Alaska: geomorphic controls on
762 bathymetry, *Permafrost and Periglacial Processes*, 23(3), 218-230, 2012.

763 Hinkel, K. M., & Arp, C.: Estimating talik depth beneath lakes in Arctic Alaska, In Proceedings,
764 7th Canadian Permafrost Conference and 68th Canadian Geotechnical Conference, pp.
765 20-23, 2015.

766 Hopkins, D. M.: Thaw lakes and thaw sinks in the Imuruk Lake area, Seward Peninsula, Alaska,
767 The Journal of Geology, 57(2), 119-131, 1949.

768 Hopkins, D. M., Karlstrom, T., Black, R., Williams, J., Pewe, T., Fernold, A., & Muller, E.:
769 Permafrost and ground water in Alaska, a shorter contribution to the general geology. US
770 Geol. Surv. Prof. Pap, 264, 1955.

771 Hunter, J. A., MacAulay, H. A., Gagné, R. M., Burns, R. A., Harrison, T. E., & Hawkins, J. P.:
772 Drained lake experiment for investigation of growth of permafrost at Illisarvik,
773 Northwest Territories—initial geophysical results, *Current research, part C. Geological*
774 *Survey of Canada, Paper*, 67-76, 1981.

775 Jeffries, M.O., Morris, K. and Liston, G.E.: A method to determine lake depth and water
776 availability on the North Slope of Alaska with spaceborne imaging radar and numerical
777 ice growth modelling. *Arctic*, pp.367-374, 1996.

778 Jeffries, M. O., Morris, K., Maksym, T., Kozlenko, N., & Tin, T.: Autumn sea ice thickness,
779 ridging and heat flux variability in and adjacent to Terra Nova Bay, Ross Sea, Antarctica,
780 *Journal of Geophysical Research: Oceans*, 106(C3), 4437-4448, 2001.

781 Johnston, G. H., & Brown, R. J. E.: Occurrence of permafrost at an Arctic lake, *Nature*,
782 211(5052), 952-953, 1966.

783 Jones, B. M., Grosse, G. D. A. C., Arp, C. D., Jones, M. C., Anthony, K. W., & Romanovsky, V.
784 E.: Modern thermokarst lake dynamics in the continuous permafrost zone, northern
785 Seward Peninsula, Alaska, *Journal of Geophysical Research: Biogeosciences*, 116(G2),
786 2011.

787 Jones, B.M., Grosse, G., Farquharson, L.M, Roy-Léveillé, P., Veremeeva A., Kanevskiy, M.Z.,
788 Gaglioti, B.V., Breen, A.L., Parsekian, A.D., Ulrich, M., and Hinkel, K.M.: Lake and
789 drained lake basin systems in lowland permafrost regions. *Nature Reviews Earth and*
790 *Environment* 3: 85-98. <https://doi.org/10.1038/s43017-021-00238-9>, 2022.

791 Jorgenson, M.T.: Thermokarst terrains. In: Shroder, J. (Editor in Chief), Giardino, R., Harbor, J.
792 (Eds.), *Treatise on Geomorphology*. Academic Press, San Diego, CA, vol. 8, *Glacial and*
793 *Periglacial Geomorphology*, pp. 313–324, 2013.

794 Jorgenson, M. T., & Shur, Y.: Evolution of lakes and basins in northern Alaska and discussion of
795 the thaw lake cycle, *Journal of Geophysical Research: Earth Surface*, 112(F2), 2007.

796 Jorgenson, T., Yoshikawa, K., Kanevskiy, M., Shur, Y., Romanovsky, V., Marchenko, S.,
797 Grosse, G., Brown, J., and Jones, B.: Permafrost characteristics of Alaska. In:
798 *Proceedings of the 9th International Conference on Permafrost, Extended Abstracts*. June
799 29–July 3, 2008, Fairbanks, AK. Kane, D.L., and Hinkel, K.M. (Eds.), *Institute of*
800 *Northern Engineering, University of Alaska Fairbanks*: 121–122, 2008.

801 Kanevskiy, M., Shur, Y., Fortier, D., Jorgenson, M. T., & Stephani, E.: Cryostratigraphy of late
802 Pleistocene syngenetic permafrost (yedoma) in northern Alaska, Ikillik River exposure.
803 *Quaternary research*, 75(3), 584-596, 2011.

804 Kanevskiy, M., Shur, Y., Jorgenson, M. T., Ping, C. L., Michaelson, G. J., Fortier, D., ... &
805 Tums koy, V.: Ground ice in the upper permafrost of the Beaufort Sea coast of Alaska,
806 Cold Regions Science and Technology, 85, 56-70, 2013.

807 Kessler, M. A., Plug, L. J., & Anthony, K. W.: Simulating the decadal - to millennial - scale
808 dynamics of morphology and sequestered carbon mobilization of two thermokarst lakes
809 in NW Alaska, Journal of Geophysical Research: Biogeosciences, 117(G2), 2012.

810 Kurylyk, B. L., & Hayashi, M.: Improved Stefan equation correction factors to accommodate
811 sensible heat storage during soil freezing or thawing. *Permafrost and Periglacial*
812 *Processes*, 27(2), 189-203, 2016.

813 Lachenbruch, A.H., Brewer, M.C., Greene, G.W., Marshall, B.V.: Temperatures in permafrost,
814 In Temperature—Its Measurement and Control in Science and Industry, 3, Herzfeld CM
815 (ed). Reinhold Publishing: New York; 791–803, 1962.

816 Lenz J, Jones BM, Wetterich S, Tjallingii R, Fritz M, Arp CD, Rudaya N, Grosse G. Impacts of
817 shore expansion and catchment characteristics on lacustrine thermokarst records in
818 permafrost lowlands, Alaska Arctic Coastal Plain. *arktos*. 2016 Dec;2(1):1-5., 2016.

819 Ling, F., & Zhang, T.: Impact of the timing and duration of seasonal snow cover on the active
820 layer and permafrost in the Alaskan Arctic, *Permafrost and Periglacial Processes*, 14(2),
821 141-150, 2003a.

822 Ling, F., and T. Zhang: Numerical simulation of permafrost thermal regime and talik
823 development under shallow thaw lakes on the Alaskan Arctic Coastal Plain, J. Geophys.
824 Res., 108(D16), 4511, doi:10.1029/2002JD003014, 2003b.

825 Livingstone, D.A.: On the orientation of lake basins, *American Journal of Science*, 252: 547–
826 554, 1954.

827 Lunardini, V.J.: *Heat Transfer in Cold Climates*, Van Nostrand Reinhold Co.: New York, NY;
828 731, 1981.

829 Mackay J.R.: The Mackenzie Delta area, N.W.T. Geographical Branch Memoir 8, Department of
830 Mines and Technical Surveys, Ottawa, 1963.

831 Mackay, J.R.: Lake stability in an ice-rich permafrost environment: examples from the western
832 Arctic coast. In: Robarts, R.D., Bothwell, M.L. (Eds.), *Aquatic Ecosystems in Semi-Arid*
833 *Regions: Implications for Resource Management*. NHRI Symposium Series 7.
834 Environment Canada, Saskatoon, Saskatchewan, pp. 1–26, 1992.

835 McClymont, A.F., Hayashi, M., Bentley, L.R. and Christensen, B.S.: Geophysical imaging and
836 thermal modeling of subsurface morphology and thaw evolution of discontinuous
837 permafrost, *Journal of Geophysical Research: Earth Surface*, 118(3), pp.1826-1837,
838 2013.

839 Ohara N., and Yamatani K.: Theoretical Stable Hydraulic Section based on the Principle of Least
840 Action. *Scientific Reports*, 9, Article number: 7957, 2019.

841 O'Neill, H. B., Roy - Leveillee, P., Lebedeva, L., & Ling, F.: Recent advances (2010-2019) in
842 the study of taliks, *Permafrost and Periglacial Processes*, 31(3), 346-357, 2020.

843 Parsekian, A. D., Creighton, A. L., Jones, B. M., & Arp, C. D.: Surface nuclear magnetic
844 resonance observations of permafrost thaw below floating, bedfast, and transitional ice
845 lakes, *Geophysics*, 84(3), EN33-EN45, 2019.

846 Painter, S. L., Coon, E. T., Atchley, A. L., Berndt, M., Garimella, R., Moulton, J. D., ... &
847 Wilson, C. J.: Integrated surface/subsurface permafrost thermal hydrology: Model
848 formulation and proof - of - concept simulations, *Water Resources Research*, 52(8),
849 6062-6077, 2016.

850 Patel, P. D.: Interface conditions in heat-conduction problems with change of phase, *AIAA*
851 *Journal*, 6(12), 2454-2454, 1968.

852 Pilon, J. A., Annan, A. P., & Davis, J. L.: Monitoring permafrost ground conditions with ground
853 probing radar (GPR), In Workshop on Permafrost Geophysics, Golden, Colorado. US
854 Army Corps of Engineers, Cold Regions Research and Engineering Laboratory, Hanover,
855 New Hampshire, CRREL Special Report (pp. 85-5), 1985.

856 Plug, L. J., & West, J. J.: Thaw lake expansion in a two - dimensional coupled model of heat
857 transfer, thaw subsidence, and mass movement, *Journal of Geophysical Research: Earth*
858 *Surface*, 114(F1), 2009.

859 Rampton, V. N.: Quaternary geology of the Yukon coastal plain, 1982.

860 Rangel R.C., A. D. Parsekian, L. M. Farquharson, B. M. Jones, N. Ohara, A. L. Creighton, B. V.
861 Gaglioti, M. Kanevskiy, A. L. Breen, H. Bergstedt, V. E. Romanovsky, and K. M.
862 Hinkel.: Geophysical Observations of Taliks Below Drained Lake Basins on the Arctic
863 Coastal Plain of Alaska. *Journal of Geophysical Research: Solid Earth* 126,
864 e2020JB020889. <https://doi.org/10.1029/2020JB020889>, 2020.

865 Reeve, D., Chadwick, A., & Fleming, C.: Coastal engineering: processes, theory and design
866 practice, CRC Press, 2018.

867 Rex, R. W.: Hydrodynamic analysis of circulation and orientation of lakes in Northern Alaska. In
868 Geology of the Arctic, Rauch GO (ed). University of Toronto Press: Toronto; 1021–
869 1043, 1961.

870 Rowland, J. C., B. J. Travis, and C. J. Wilson: The role of advective heat transport in talik
871 development beneath lakes and ponds in discontinuous permafrost, *Geophys. Res. Lett.*,
872 38, L17504, doi:10.1029/2011GL048497, 2011.

873 Roy-Leveillee, P., & Burn, C. R.: Near - shore talik development beneath shallow water in
874 expanding thermokarst lakes, Old Crow Flats, Yukon, *Journal of Geophysical Research:*
875 *Earth Surface*, 122(5), 1070-1089, 2017.

876 Schirrmeister, L., Froese, D., Tums koy, V., Grosse, G., and Wetterich, S.: Yedoma: Late
877 Pleistocene ice-rich syngenetic permafrost of Beringia. *Encyclopedia of Quaternary*
878 *Science*, 2nd ed., pp. 542–552, 2013.

879 Schuur, E. A., McGuire, A. D., Schädel, C., Grosse, G., Harden, J. W., Hayes, D. J., ... & Natali,
880 S. M.: Climate change and the permafrost carbon feedback. *Nature*, 520(7546), 171-179,
881 2015.

882 Schwamborn, G., Andreev, A., Rachold, V., Hubberten, H. W., Grigoriev, M. N., Tums koy,
883 V., ... & Dorozkhina, M. V.: Evolution of Lake Nikolay, Arga Island, Western Lena
884 River delta, during late Pleistocene and Holocene time, *Polarforschung*, 70, 69-82, 2000.

885 Séjourné, A., Costard, F., Fedorov, A., Gargani, J., Skorve, J., Massé, M., & Mège, D.:
886 Evolution of the banks of thermokarst lakes in Central Yakutia (Central Siberia) due to

887 retrogressive thaw slump activity controlled by insolation. *Geomorphology*, 241, 31-40,
888 2015.

889 Sellmann, P. V.: *The classification and geomorphic implications of thaw lakes on the Arctic*
890 *Coastal Plain, Alaska* (Vol. 344), US Department of Defense, Department of the Army,
891 Corps of Engineers, Cold Regions Research and Engineering Laboratory, Report. 21 pp,
892 1975.

893 Shur, Y., and Osterkamp, T.: Thermokarst. Report INE 06.11. University of Alaska Fairbanks,
894 Institute of Northern Engineering, Fairbanks, AK (50 pp.), 2007.

895 Silvester, R., & Hsu, J. R.: Coastal Stabilization, Advanced Series on Ocean Engineering, Vol.
896 14, 1997.

897 Singer-Loginova, I., & Singer, H. M.: The phase field technique for modeling multiphase
898 materials. *Reports on progress in physics*, 71(10), 106501, 2008.

899 Stefan J.: Über die Theorie der Eisbildung, insbesondere über die Eisbildung im Polarmee.
900 *Annals of Physics and Chemistry* 42: 269–286, 1891.

901 Sullivan, T. D., Parsekian, A. D., Sharp, J., Hanke, P. J., Thalasso, F., Shapley, M., ... & Walter
902 Anthony, K.: Influence of permafrost thaw on an extreme geologic methane seep.
903 *Permafrost and Periglacial Processes*, 2021.

904 Tomirdiaro, S. V.: Evolution of lowland landscapes in northeastern Asia during late Quaternary
905 time, In *Paleoecology of Beringia* (pp. 29-37). Academic Press, 1982.

906 van Everdingen, R.O. (Ed.): Multi-Language Glossary of Permafrost and Related Ground-ice
907 Terms, International Permafrost Association, The Arctic Institute of North America,
908 University of Calgary, Calgary, 268 pp, 1998.

909 West, J. J., and L. J. Plug: Time-dependent morphology of thaw lakes and taliks in deep and
910 shallow ground ice, *J. Geophys. Res.*, 113, F01009, doi:10.1029/2006JF000696, 2008.

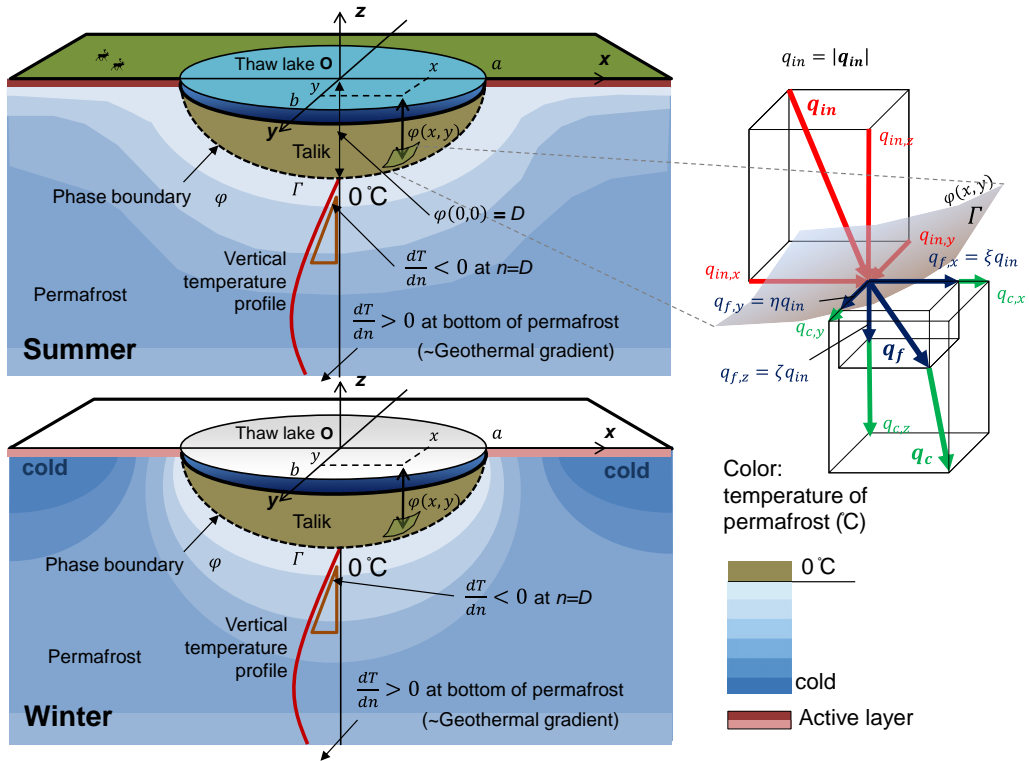
911 Westermann, S., Schuler, T. V., Gislås, K., & Etzelmüller, B.: Transient thermal modeling of
912 permafrost conditions in Southern Norway, *The Cryosphere*, 7(2), 719-739, 2013.

913 Table 1: Computed incoming heat flux with the estimated parameters

Parameter	Estimates	Unit	Note
Porosity	0.18		Sandstone >15 m deep; Creighton et al., 2018
Thermal conductivity of permafrost	2.20	W/(m·K)	From porosity and typical thermal properties of ice and mineral in this region
Talik depth, D	88.0	m	Fitted ellipsoid
Talik width (radius), a	514.8	m	Fitted ellipsoid
Aspect ratio, D/a	0.1709		Fitted ellipsoid
Geothermal gradient	0.0250	K/m	Kessler et al., 2012
dT/dz at the talik bottom	-0.0259	K/m	From Mackay model (1962)
Basin average heat flux, q_{in}	0.0689	W/m ²	Computed from Equation (29)

914

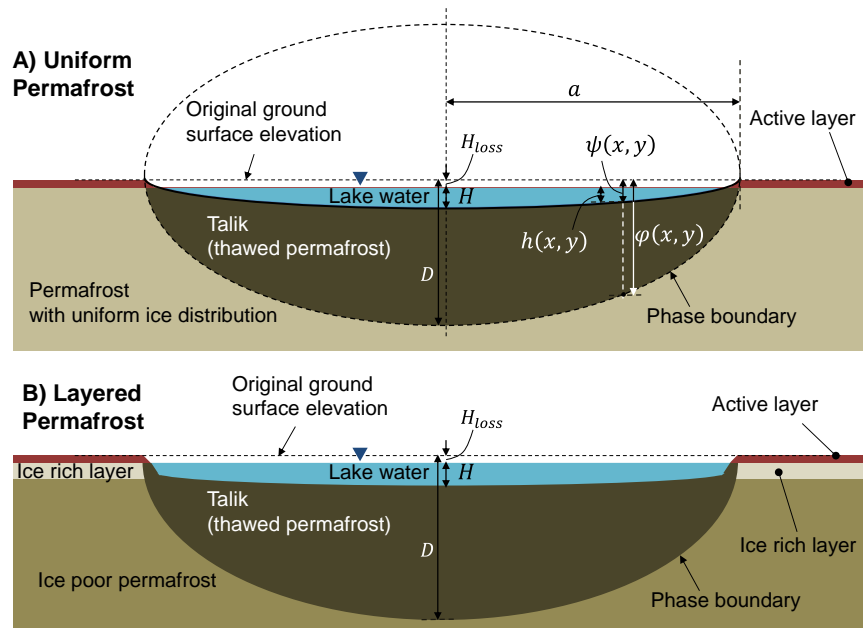
915



916

917 Figure 1: Definitions of variables associating with the overall shape of phase boundary φ during warm
 918 (Upper left panel) and cold seasons (Lower left panel) and incoming and outgoing heat transfers on
 919 $\varphi(x, y)$ (Right panel). Incoming heat (red colored vector) is perpendicular to the phase boundary
 920 $\varphi(x, y)$ while thaw direction (blue colored vector) is modified by the anisotropic heat conduction (green
 921 colored vector) in the permafrost.

922

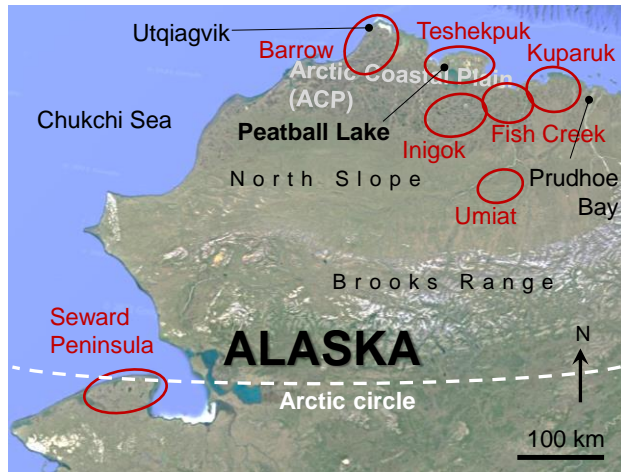


923

924 Figure 2: Lake bathymetry models for a thermokarst lake and the talik underneath based on the quasi-
 925 steady state. (A) The lake bathymetry is proportional to the talik geometry with uniform ice distribution.

926 (B) The lake bathymetry tends to have a flat bottom due to the widespread ice-rich layer near the surface.

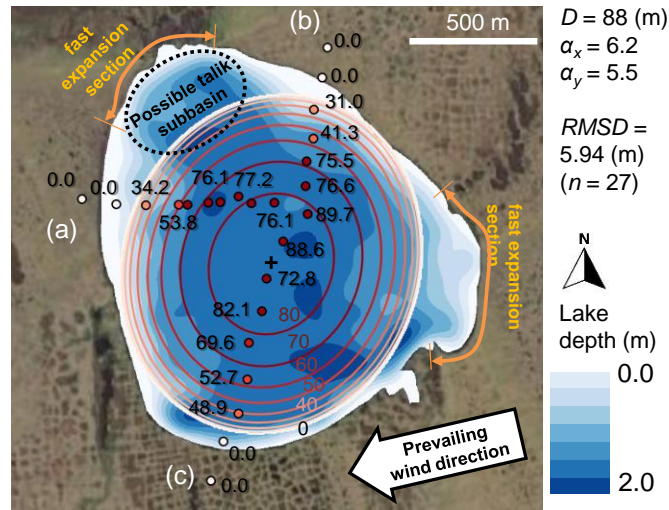
927



928

929 Figure 3: Map of the study area: Peatball Lake and subregions for lake characterization (red).

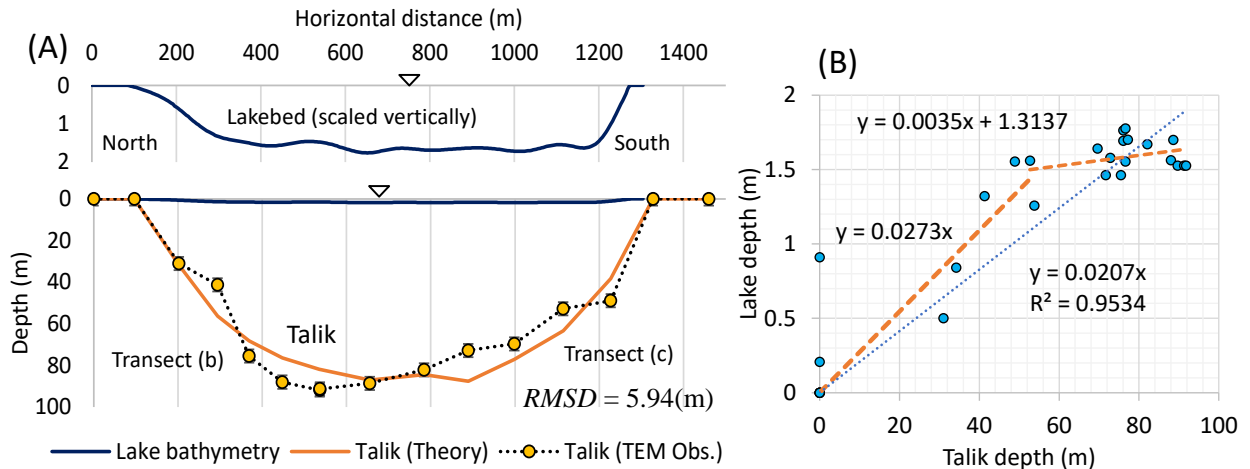
930



931

932 Figure 4: The theoretically extrapolated talik thickness map (contour lines) based on 27 TEM soundings
 933 (dots) in Peatball Lake, ACP of Alaska. The red contour lines and the observation points are consistent.
 934 The corresponding observed lake bathymetry (adopted from Lenz et al., 2016) is also included in blue
 935 gradation. The TEM sounding transects start on the lakeshore and end near the center of the lake.

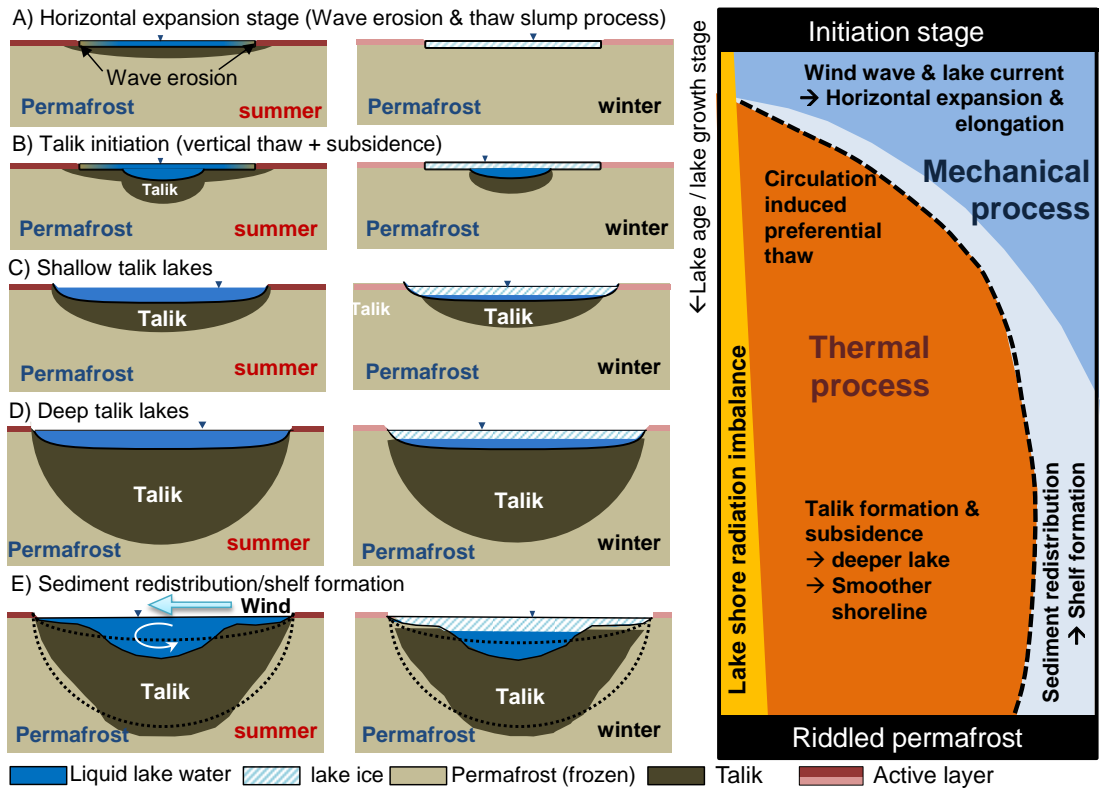
936



937

938 Figure 5: Cross sectional comparisons of the lakebed and the talik profiles along two TEM transects (b)
 939 through (c) (Lenz et al., 2016) in Peatball Lake. Panel (B) displays the cross plot of the observed talik
 940 and lake depths at all 27 TEM data points.

941



942

943

944

945

946

947

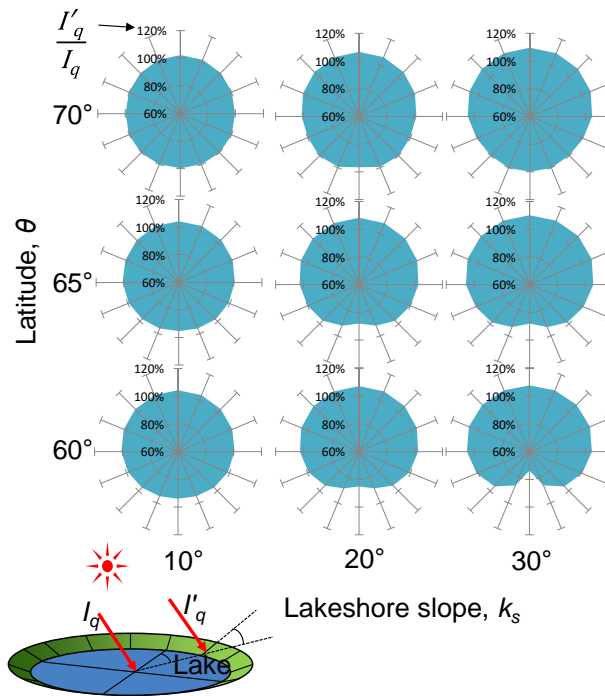
948

949

950

951

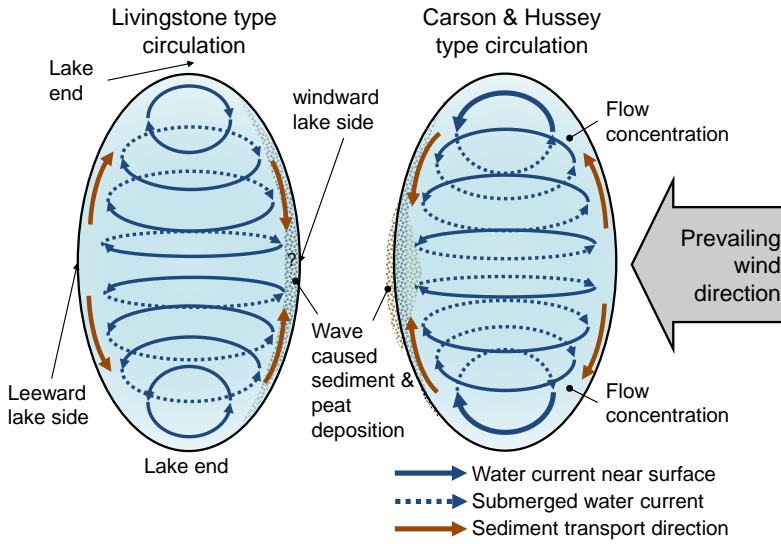
Figure 6: Combined hypothetical models of thermokarst lake evolution and diagram of major influencing factors through time. The left column represents summer conditions, the center column represents winter conditions, and the right column indicates the corresponding importance of mechanical vs. thermal processes through time as the lake ages (top is younger, bottom is older). Row (A) indicates the early processes under bedfast ice conditions before talik initiation. Row (B) shows the onset of vertical thaw and subsidence as talik begins to develop. Row (C) shows early, shallow talik growth conditions. Row (D) indicates later stage processes on deepened talik due to vertical thaw. Row (E) is the mature stage of development when complex bathymetry has set in as a result of sediment transport.



952

953 Figure 7: Computed mean daily potential solar radiation on sloping lakeshore relative to the flat surface
 954 during summer period (June-August) with respect to latitude. I_q is the potential solar radiation on a flat
 955 surface, and I'_q is radiation on sloping lakeshore.

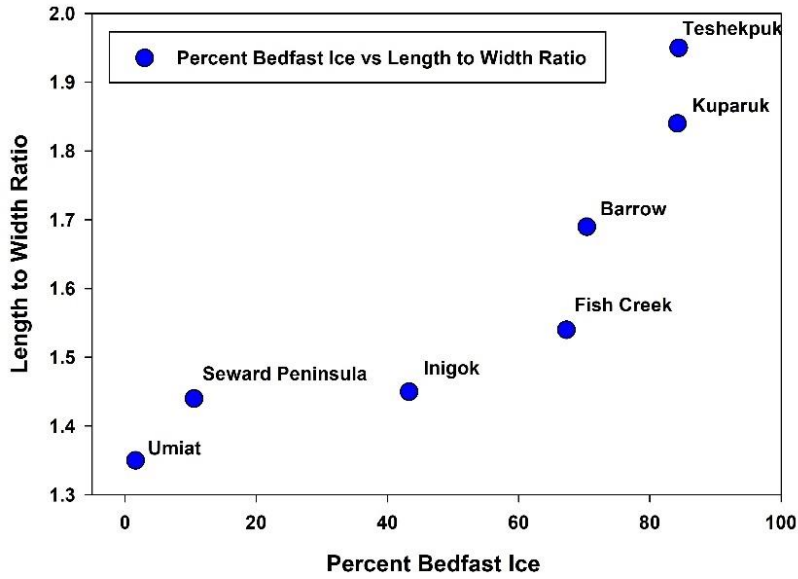
956



957

958 Figure 8: Two distinctive lake water circulation patterns created by unidirectional wind. Livingstone type
 959 circulation (Left) and Carson & Hussey type circulation (Right) cause opposite flow directions around
 960 lake ends. This also results in difference in sediment and peat deposition patterns.

961



962

963 Figure 9: Comparison of Length to Width ratio versus the percent of a particular region exhibiting a
 964 bedfast lake ice regime for seven study areas in Arctic Alaska. This analysis is based on SAR-satellite
 965 remote-sensing data presented in Engram et al. (2018). Lakes that are more elliptical in shape tend to
 966 occur where the majority of the lakes in the area freeze to their bed and thus likely do not have a talik.
 967 Lakes that are more circular in shape tend to occur where the majority of lakes in an area do not freeze to
 968 their bed and thus likely have a sub-lake talik.

969